Three-dimensional Weyl hourglass networks in the nonsymmorphic half-metal Mg_2VO_4

Haopeng Zhang, Xiaoming Zhang,* Tingli He, Xuefang Dai, Ying Liu, and Guodong Liu†
State Key Laboratory of Reliability and Intelligence of Electrical Equipment, Hebei University of Technology, Tianjin 300130, China and School of Materials Science and Engineering, Hebei University of Technology, Tianjin 300130, China

Liying Wang
Tianjin Key Laboratory of Low Dimensional Materials Physics and Preparation Technology, School of science, Tianjin University, Tianjin 300354, People's Republic of China

Ying Zhang‡
Physics Department, Beijing Normal University, Beijing 100875, China

(Received 28 July 2020; accepted 25 September 2020; published 13 October 2020)

Fermions with hourglass dispersions have been hotly studied in a nonmagnetic system currently. However, magnetic ones have been rarely discussed because of the scarcity of excellent candidate materials. Here, promoted by first-principles and symmetry analysis, we propose the presence of novel hourglass nodal networks in a nonsymmorphic half-metal Mg_2VO_4 that is constructed by three touching hourglass nodal lines at mutually intersecting planes in the extended Brillouin zone. Unlike previous hourglass semimetals in nonmagnetic materials, the material proposed here has a ferromagnetic half-metallic state; thus, the hourglass nodal networks are fully spin polarized. We also show that the hourglass nodal networks manifest spin-polarized drumhead surface states. We demonstrate the hourglass nodal networks are enforced by nonsymmorphic symmetry, and effective models are constructed. We further show that the novel topological phase of Mg_2VO_4 is robust against lattice strain and electron correlation effects. Our work provides a good platform to investigate novel hourglass fermions from nonsymmorphic symmetries in magnetic system.

DOI: 10.1103/PhysRevB.102.155116

I. INTRODUCTION

Since the discovery of Weyl and Dirac semimetals [1–14], topological semimetals have been a current focus in condensed matter physics. In these materials, the band structure exhibits band crossings near the Fermi level. The fermionic excitations around band crossings can hold distinct types of dispersions, and their unique topological characteristics acquire novel transport and optical phenomena [15–21]. Diverse topological semimetals may show band crossings with different dimensions in the reciprocal space, which include discrete nodal points [22–29], continuous nodal lines, and nodal surfaces [9,30–40]. Nodal line semimetals, which are characterized with topologically nontrivial Berry phase and drumhead surface states, have attracted considerable attention currently. A large number of nodal line semimetals are proposed [40–48], and some are convinced by experiments [49–52]. Among these examples, most nodal lines can be annihilated without changing the symmetry and are vulnerable against spin-orbit coupling (SOC), namely accidental nodal lines [53–55].

Nonsymmorphic symmetries, which involve fractional lattice translations, have been hotly discussed to stabilize symmetry-enforced band crossings [23,56–60]. Their influences manifest in two aspects. For the first one, they can enable the band degeneracy robust against SOC. Some stable nonsymmorphic Weyl (double degeneracy) and Dirac (fourfold degeneracy) nodal lines have already been proposed under SOC [53,61–63]. Second, multiple energy bands could be entangled together in topological systems with nonsymmorphic symmetries. This gives rise to the potential formation of new fermionic states. Hourglass fermions are one typical example, where four bands are entangled into groups with hourglass-shaped dispersions [64–67]. For another example, under nonsymmorphic symmetry, multiple nodal lines can form various configurations such as Hopf link, nodal box, nodal chain, and nodal net [45,54,68–74]. So far, nonsymmorphic topological semimetals are mostly proposed in a nonmagnetic system, while magnetic candidates are still limited. Therefore, it is very meaningful to explore nonsymmorphic topological semimetals in a magnetic system for expediting the investigations on their intriguing properties and exploring potential applications in spintronics as well.

In current work, we predict a remarkable topological phase in magnetic compound Mg_2VO_4 that enabled by nonsymmorphic symmetry. The material intrinsically shows a ferromagnetic half-metallic band structure, where only bands from the spin up channel exist near the Fermi level. Four

*zhangxiaoming87@hebut.edu.cn
†gdliu1978@126.com
‡yingzhang@bnu.edu.cn

spin up bands are entangled into groups and form three types of hourglass nodal lines (HNLs). These HNLs are conjunct together that further form hourglass networks in the three-dimensional (3D) Brillouin zone (BZ). The hourglass networks are fully spin polarized, which are different from those proposed in nonmagnetic materials. The protection mechanism and the effective models for the hourglass networks are fully addressed. The hourglass networks locate almost at the Fermi level and show clean drumhead surface states, which can facilitate their detections in experiments. The spin-orbit coupling (SOC), lattice strain, and electron correlation effects on the hourglass networks are discussed. This work suggests Mg_2VO_4 compound is a good material candidate for studying the basic physics of hourglass fermions in a magnetic system.

II. COMPUTATIONAL METHOD

The first-principle calculation that we used is based on the density functional theory (DFT), which is implemented in the Vienna *ab initio* simulation package (VASP) [75,76]. The correlation potential is chosen as the generalized gradient approximation (GGA) with Perdew-Burke-Ernzerhof (PBE) [77]. The plane-wave cutoff energy was set to 500 eV. A Monkhorst-Pack k-point mesh [78] of size $11 \times 11 \times 11$ was used for the BZ sampling. Energy and force convergence criteria were set as 10^{-6} eV and 0.01 eV/Å, respectively. To account for the correlation effects for transition-metal elements, the DFT $+U$ method [79,80] was used to calculate the band structures. The effective U values between 0 and 6 eV have been tested for the V $3d$ orbitals. For the topological band structure shown in the following sections, the effective U value is chosen as 4 eV. To be noted, the conclusion of the work would not change if we slightly shift the U values. The surface states are calculated by using the WANNIERTOOLS package [81].

III. CRYSTAL STRUCTURE, SYMMETRY, AND MAGNETIC CONFIGURATION

Compound Mg_2VO_4 is an existing material and has already been synthesized by different experimental technologies [82–84]. The Mg_2VO_4 crystal structure belongs to a face-centered cubic Bravais lattice, with the space group $Fd\bar{3}m$ (No. 227). Figure 1(a) shows the conventional crystal structure of Mg_2VO_4 compound. The cubic unit cell of Mg_2VO_4 totally contains 56 atoms. Among them, 32 O atoms locate at the 32e (0.373, 0.373, 0.373) Wyckoff position, 16 Mg atoms occupy at the 16d (0.125, 0.125, 0.125) Wyckoff position, and 8 V atoms situate at the 8a (0.5, 0.5, 0.5) Wyckoff position. The conventional unit cell is composed of a cubic framework of V atoms. Each V atom is surrounded by four O atoms, which form a tetrahedral local crystal. The Mg atoms are inserted into the cubic framework. Each Mg atom bonds with six O atoms to form the Mg-O_6 octahedron. The primitive unit cell contains two formula units of Mg_2VO_4, which shows in Fig. 1(b). The optimized lattice parameters are basically consistent with the experimental results [82–84]. The optimized lattice constant is

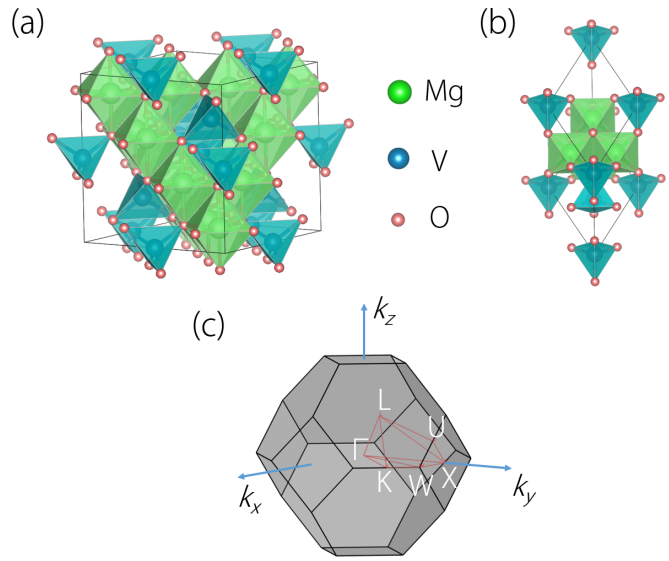

FIG. 1. (a) Conventional unit cell and (b) the primitive unit cell of crystal structure for Mg_2VO_4. (c) The corresponding Brillouin zone with the considered high-symmetry paths.

$a = b = c = 8.458$ Å, which is applied in electronic structure calculations.

There are three nonsymmorphic glide planes involving fractional lattice translations, G_z: $(x, y, z) \rightarrow (x + 1/4, y + 3/4, -z + 1/2)$, G_{101}: $(x, y, z) \rightarrow (-y + 1/4, x + 3/4, -z + 1/2)$, and G_{110}: $(x, y, z) \rightarrow (-x + 1/4, -y + 3/4, z + 1/2)$. Combining these three nonsymmorphic symmetry operations leads to the twofold rotation C_2. These symmetries are important for our discussion below.

To obtain the ground magnetic state in Mg_2VO_4, we have considered three magnetic arrangements of V atoms, which include nonmagnetic (NM), ferromagnetic (FM) and antiferromagnetic (AFM). In addition, we have also considered three potential magnetic ordering directions including [001], [110], and [111] in the FM and AFM states. In Table I, we show the calculated total energies for the considered magnetic arrangements in Mg_2VO_4. We can find that the FM state with the [111] magnetization is the most energetically stable. In addition, we have also checked the ground magnetic states with U values in the range of 0–6 eV. We find Mg_2VO_4 compound always shows the FM ground state. In the following, we investigate the band topology of Mg_2VO_4 in the FM ground state.

TABLE I. Total energy E_{tot} per unit cell (in eV, relative to that of the FM_{111} ground state), as well as magnetic moment M (in units of μ_B) per V atom. The values are calculated by the GGA+SOC method with $U = 4.0$ eV.

	FM_{001}	FM_{110}	FM_{111}	AFM_{001}	AFM_{110}	AFM_{111}
Energy/eV	0.0001	0.0002	0	0.0344	0.0075	0.0342
M_x/μ_B	0.0010	0.7880	0.6430	0.0010	0.7830	0.6280
M_y/μ_B	0.0010	0.7880	0.6430	0.0020	0.7820	0.6310
M_z/μ_B	1.1140	0.0010	0.6430	1.0940	0.0010	0.6370

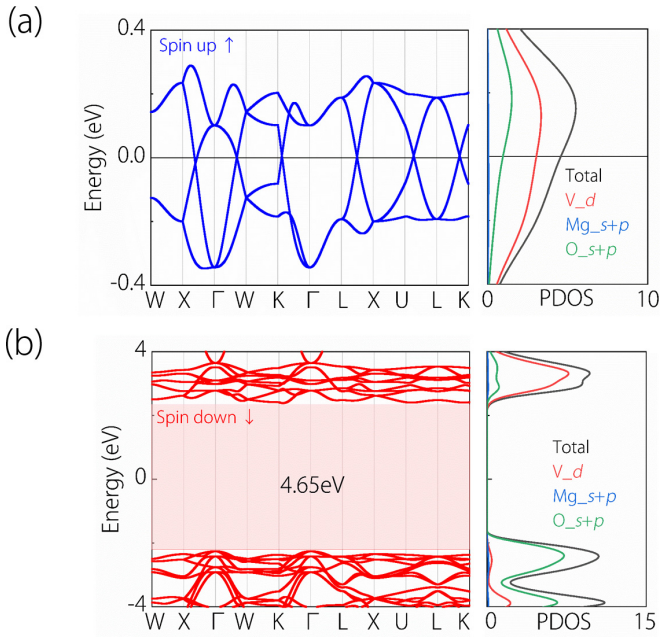

FIG. 2. The electronic band structures and projected density of states (PDOS) of Mg_2VO_4 compound in the absence of SOC. (a) is for the spin up case, showing a metallic character with bands crossing the Fermi level. (b) is for the spin down case, exhibiting an insulating character with a big band gap of 4.65 eV.

IV. FULLY SPIN-POLARIZED HOURGLASS NETWORKS

We start with the electronic structures of Mg_2VO_4 compound in the absence of SOC. The band structure and projected density of states (PDOSs) in the spin up and spin down channels are shown in Figs. 2(a) and 2(b), respectively. It is very interesting to find that the band structures in the spin up and spin down states exhibit completely different conducting behaviors. In the spin up channel, we can observe four bands entangle together near the Fermi level, and the band structure shows the metallic character. However, the bands in the spin down channel exhibit an insulating signature with an energy gap of 4.65 eV around the Fermi level. These results show that the Mg_2VO_4 compound is a half-metal phase, where the conducting electrons have a 100% spin polarization. A further observation finds several band crossings in the spin up band structure, as shown in Fig. 2(a). Especially, band crossings show hourglass dispersions in the X-Γ, Γ-W, and L-X paths. These novel band crossings will be discussed in detail below. From the provided PDOSs, we find the electron states near the Fermi level are mostly contributed by the d orbitals of V element. Considering that GGA functional usually underestimates potential band gaps, here we have also checked the band structure under the Heyd-Scuseria-Ernzerhof (HSE06) functional [77,85]. We show the band structure in the spin up channel in Fig. 3. We can observe that the band crossings near the Fermi level are retained under HSE06 calculation.

We here review the general characters of the band structure in the spin up channel. As shown in Fig. 2(a), there are totally six band crossing points near the Fermi level, which happen in the X-Γ, Γ-W, K-Γ, L-X, U-L, and L-K paths, respectively. After a careful scan on the band structures, we

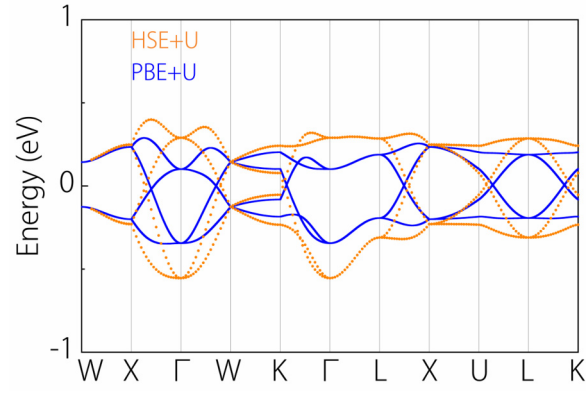

FIG. 3. The band structure of Mg_2VO_4 in the spin up channel along high-symmetry k paths using HSE and PBE calculation.

find these crossing points are not isolated but belong to three hourglass nodal lines (HNLs). Figures 4(a)–4(c) show the orbital-component band structures for the crossing points. In each case, we find four bands are entangled into two groups and show the hourglass-shaped dispersions. These bands are mostly contributed by the $V-d_{xz}$, $V-d_{yz}$, and $V-d_{x^2-y^2}$ orbitals. We can clearly observe the band inversion feature near these crossing regions, which indicates the potential nontrivial band topology in Mg_2VO_4 compound.

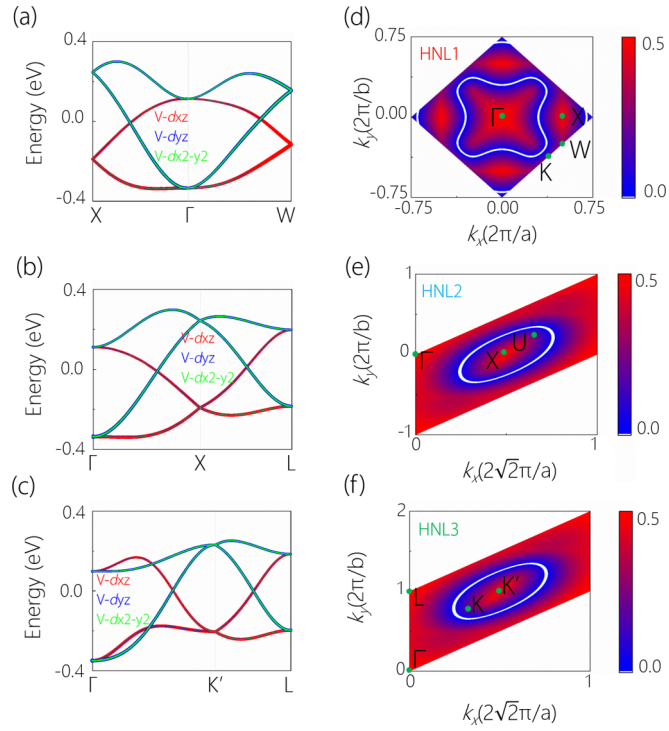

FIG. 4. (a)–(c) Orbital-projected band structure of Mg_2VO_4, including V-d_{xz} orbital (red), V-d_{yz} orbital (blue) and V-$d_{x^2-y^2}$ orbital (green). (d)–(f) show the profiles of hourglass nodal lines in $k_z = 0$ plane, k_{x-z} plane, and $k_{x-y} = 0$ plane, which are labeled as HNL1, HNL2, and HNL3, respectively. In (d)–(f), the color map indicates the local gap between two crossing bands.

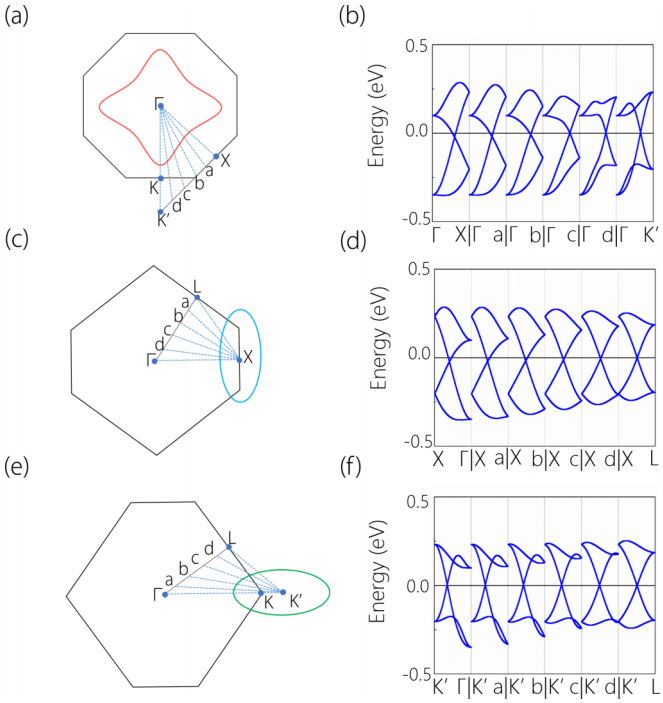

FIG. 5. (a) Illustration of the HNL1 in the $k_z = 0$ plane. The points a, b, c, and d are equally spaced between X and K′. (c) Schematic illustration of the HNL2 in the k_{x-z} plane. The points a, b, c, and d are equally spaced between Γ and L. (c) Schematic illustration of the HNL3 in the k_{x-y} plane. The points a, b, c, and d are equally spaced between Γ and L. (b), (d), and (f) are band structures along the k paths as indicated in (a), (c), and (e), respectively.

The profiles of the three HNLs are shown in Figs. 4(d), 4(e) and 4(f). For clarity, we here denote them as HNL1, HNL2, and HNL3, respectively. HNL1 situates in the $k_z = 0$ plane, centering the Γ point in the BZ. It manifests a petaloid profile, as shown in Fig. 4(d). HNL2 and HNL3 both show the elliptical profiles but have distinct locations. HNL2 locates in the Γ-X-L plane (denoted as k_{x-z} plane), centering the X point [see Fig. 4(e)], while HNL3 locates in the Γ-K-L plane (k_{x-y} plane), centering the K′ point [see Fig. 4(f)].

To examine band dispersions at other regions of the HNLs, we have selected several other k paths in these planes. As shown in Figs. 5(a), 5(c) and 5(e), the selected k paths all traverse the HNLs. The corresponding band structures are displayed in Figs. 5(b), 5(d) and 5(f), respectively. We can observe that all the k paths show hourglass band dispersions. These results have fully verified the HNL signature in Mg_2VO_4 compound.

To capture the topology signature of the HNLs, we calculate the Berry phases for a closed loop surrounding each HNL as

$$P_B = \oint_L A(k) \cdot dk. \tag{1}$$

Here, $A(k) = -i\langle\, \varphi(k) \mid \nabla_k \mid \varphi(k) \,\rangle$ denotes the Berry connection, and $\varphi(k)$ is the wave function. After numerical calculations, we find that these HNLs all give the Berry phase of $P_B = \pi$, which shows that they are topologically nontrivial. We notice that all the HNLs locate in the mirror-invariant

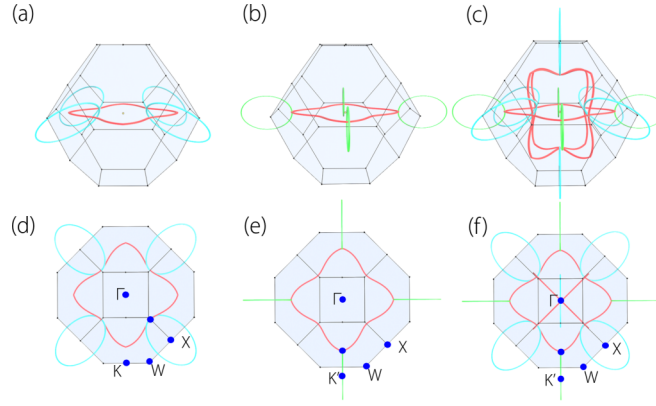

FIG. 6. (a) Schematic illustration of the outer nodal chain formed by HNL1 (the red loop) and HNL2 (the light blue loop). (b) Schematic illustration of the outer nodal chain formed by HNL1 (the red loop) and HNL3 (the green loop). (c) Schematic illustration of the 3D hourglass networks formed by HNL1, HNL2, and HNL3. (d)–(f) are the corresponding top views of (a)–(c).

planes. For HNL1, it situates in the $k_z = 0$ plane, which is found to be protected by the glide mirror symmetry G_z involving half the lattice translations. We have calculated the eigenvalues for the crossing bands and find they possess opposite eigenvalues. This ensures the formation of nodal line without opening gaps. Similarly, we find HNL2 and HNL3 are also protected by glide mirror symmetries, which are G_{101} and G_{110}, respectively. Both G_{101} and G_{110} also preserve the fractional lattice translations.

It is very interesting to note that the HNLs are not isolated but connected together to form 3D nodal networks in the BZ. The configurations of the nodal networks are depicted by the 3D model in Fig. 6(c), where HNL1 is shown by the red loops, which lie in the $k_x = 0$, $k_y = 0$, and $k_z = 0$ planes. HNL2 are shown as the blue loops, locating in the k_{x-y}, k_{y-z}, and k_{x-z} planes. HNL3 are shown as the green loops, which situate in the k_{x-y}, k_{y-z}, and k_{x-z} planes. The complex nodal networks can be simply decomposed into several nodal chains. First, three loops of HNL1 form an inner nodal chain, as shown by the red loops in Fig. 6(c). Second, HNL1 and HNL2 connect at the same point in the Γ-X path, which form an outer nodal chain structure, as shown in Fig. 6(a). Such a connection can be clearly identified by the top view of the model in Fig. 6(d). Third, HNL1 and HNL3 are also not isolated but form another outer chain. They share the same nodal point in the Γ-K path, as shown in Figs. 6(b) and 6(e). These nodal chains entangle together, thereby forming the 3D nodal networks, as shown in Figs. 6(c) and 6(f).

Now, we investigate the surface states corresponding to the nodal networks. Figure 7(a) displays the projection of the nodal networks onto the (001) surface in Mg_2VO_4 compound. We show the constant energy contours at the Fermi level for the (001) surface states in Fig. 7(b). We can observe several sharp surface bands, which are in fact the drumhead surface states. To more clearly characterize the relationship between HNLs and the projected surface states, we outline the profiles of HNL1, HNL2, and HNL3 when projected onto the (001) surface. As shown in Fig. 7(c), we can observe that the sharp

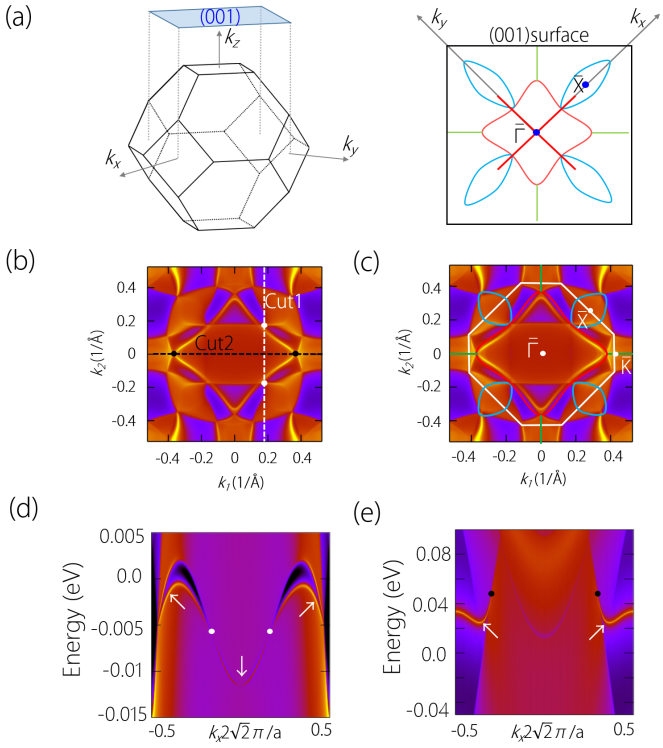

FIG. 7. (a) The bulk BZ and the projection of hourglass networks onto the (001) surface. (b) The (001) surface states in the first BZ at the Fermi level. The sharp features are the surface states. (c) The (001) surface states with the profiles of project hourglass networks provided. (d) and (e) are surface band structures along cut1 and cut2 indicated in (b), where the drumhead surface states are pointed by the arrows.

surface bands originate from the nodal networks. In addition, we have selected two paths crossing through distinct tangent points between the HNLs [cut1 and cut2 in Fig. 7(b)]. We show the corresponding surface band structures in Figs. 7(d) and 7(e). In these cases, the drumhead surface states can be clearly identified.

V. ROBUSTNESS OF HOURGLASS NETWORKS

In this section, we investigate the robustness of the hourglass networks. We first consider the SOC effects on the electronic band structure. As discussed above, the three HNLs are protected by specific glide mirror symmetries. In Mg_2VO_4 compound, the ground magnetic ordering is along in the [111] direction, which will break all the glide mirror symmetries displayed above. Therefore, all the HNLs are gapped under SOC, as shown in the band structures in Fig. 8(a). However, the SOC effects in Mg_2VO_4 compound are not quite pronounced, and the SOC gaps are only 1.79–10.19 meV. To be noted, these SOC gaps are smaller than former proposed hourglass nets in Ag_2BiO_3 [86,87].

We notice Mg_2VO_4 compound has a soft magnetism, since the energy difference among different magnetization directions is very small. The magnetization can be easily tuned by external strain. Then, if the magnetization is applied in a specific direction which preserves one certain glide mirror symmetry, some HNLs can be retained. We show this point

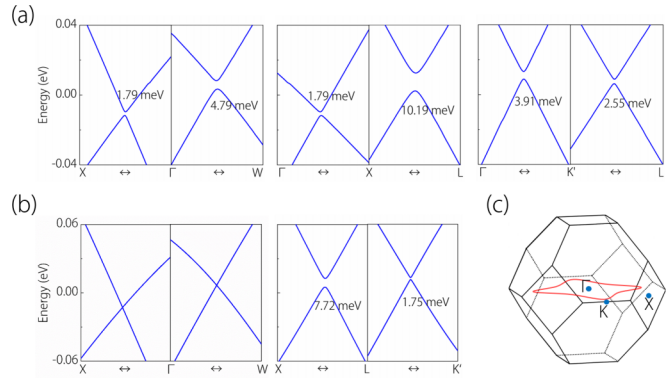

FIG. 8. (a) Electronic band structure of Mg_2VO_4 with SOC under the [111] magnetization. The size of SOC gaps are indicated. (b) Electronic band structure of Mg_2VO_4 with SOC under the [001] magnetization. (c) Schematic illustration of a single HNL in the $k_z = 0$ plane under the [001] magnetization.

by applying the [001] magnetization. The corresponding band structure under SOC is shown in Fig. 8(b). We find HNL1 in the $k_z = 0$ plane can retain, since the glide mirror symmetry G_z preserves in the [001] magnetization. As a result, the hourglass networks transform into an hourglass line, as shown in Fig. 8(c).

Unlike accidental nodal lines, HNLs are robust against perturbations as long as the nonsymmorphic glide planes preserve. We show this point by applying lattice strains and shifting electron correlation strength. Beside the HNLs, we are also concerned about the half-metallicity in Mg_2VO_4 compound, which ensures the fully spin-polarized conducting electrons. In Fig. 9(a), we show the changes of the conduction band minimum (CBM) and the valence band maximum (VBM) in the spin down channel under different strains. To

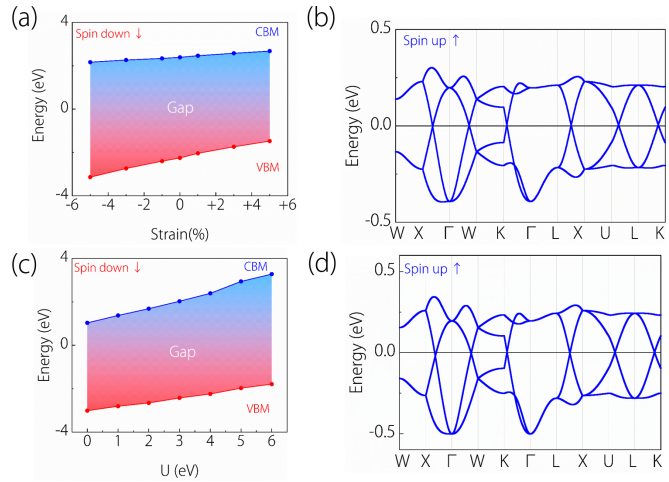

FIG. 9. (a) In the spin down channel, the curves of valence band maximum (VBM) and conduction band minimum (CBM) under different strains. The middle area formed by the curves represents the band gap. (b) The band structure of Mg_2VO_4 compound in the spin-up channel with strain at +6%. (c) Variation curves of VBM and CBM in the spin down channel under different U values. (d) The spin-up band structure under $U = 6$ eV.

be noted, we here apply the hydrostatic strain to ensure the existence of all glide symmetries. The tensile and compressive strains are shown by "+" and "−," respectively. As shown in Fig. 9(a), we find both CBM and VBM will not touch the Fermi level during the stain shifting from −5% to +5%. This suggests the half-metallicity in Mg_2VO_4 is very robust against strain. More importantly, we find that all the band crossings of the 3D hourglass networks in the spin up channel can also retain under strain. Here, we take the band structure in spin up under +5% strain as an example, and the result is shown in Fig. 9(b). Similarly, we have also investigated the impacts of electron correlation strength on the half-metallicity and hourglass networks in Mg_2VO_4. The results are shown in Figs. 9(c) and 9(d). We can find that the electronic structure is also quite robust against the electron correlation effects by shifting the U values from 0 to 6 eV. This phenomenon can be understood from the crystal field view. In Mg_2VO_4 compound, the bonding between V and O atoms forms the V-O_4 tetrahedron local structure. Under the tetrahedral crystal field, the V-3d orbitals split into two parts: the triple degenerate t_{2g} orbitals and the double degenerate e_g orbitals. Further exchange splitting among these d orbitals would break the time-reversal symmetry and lead to the spin degeneracy, thereby forming the half-metal band structure. In Mg_2VO_4 compound, each V atom transforms four valence electrons to the neighboring O atoms and only one valence electron is left. As a result, the V^{4+} is just half-filled in the e_g orbital. Such half-filled configuration leads to the four entangled band structure around the Fermi level, which is not very sensitive to the choice of the U values. Such high robustness of half-metallicity and hourglass networks quite facilitate their experimental detections.

VI. EFFECTIVE MODEL

As discussed above, the nodal networks consist of connections among HNL1, HNL2, and HNL3. We first prove the presence of HNL1 centered at the Γ point. It is protected by glide mirror $G_z : (x + 3/4, y + 1/4, -z + 1/2)$. To protect the nodal ring, the two crossing bands should have opposite eigenvalues of G_z, which have already been verified by our DFT calculations such that G_z has a matrix representation as $G_z = \sigma_z$. Generally, we consider the effective Hamiltonian is given by

$$\mathcal{H}_\Gamma = \sum_{i=x,y,z} d_i(\boldsymbol{k})\sigma_i, \tag{2}$$

where σ is the Pauli matrix. As we know that

$$G_z\mathcal{H}_\Gamma G_z^{-1} = \mathcal{H}_\Gamma(k_x, k_y, -k_z), \tag{3}$$

to satisfy this commutation relation, it requires that

$$d_{x,y}(k_x, k_y, k_z) = -d_{x,y}(k_x, k_y, -k_z), \tag{4}$$

$$d_z(k_x, k_y, k_z) = d_z(k_x, k_y, -k_z). \tag{5}$$

According to the DFT result, the nodal ring lies on plane $k_z = 0$, such that Eq. (4) vanishes. Therefore, the nodal ring is determined by $d_z(\boldsymbol{k})$. We consider up to the second order of $\boldsymbol{k}$, then we have

$$d_z(\boldsymbol{k}) = M_0 + \alpha k_x^2 + \beta k_y^2 + \gamma k_z^2, \tag{6}$$

with $M_0\alpha < 0$, $M_0\beta < 0$, which indicates a nodal ring on plane $k_z = 0$. The remaining operations further constrain the shape of nodal ring, but only the mirror operation G_z determines its existence.

Similar discussion is also applied to HNL2 and HNL3 on the $k_x = k_y$ ($k_x = k_z$) plane. Glide mirror G_{110} (G_{101}) is predicted to have opposite eigenvalues for the two crossing bands. Such that the glide mirror is given by $G_{110} = \sigma_z$ ($G_{101} = \sigma_z$), it also describes a nodal ring on the corresponding plane. Specifically, the nodal ring is determined by $d_z(-k, -k, k_z) = M_0 + \alpha' k^2 + \gamma k_z^2$ ($d_z(-k, k_y, -k) = M_0 + \alpha' k^2 + \beta k_y^2$) for the $k_x = k_y$ ($k_x = k_z$) plane. Therefore, we have proved that there are three types of nodal rings, as shown in Fig. 4(a), 4(c) and 4(e). Among them, HNL1 and HNL2 touch at some point along the Γ-X direction, and HNL1 and HNL3 touch the Γ-K direction. They finally can form the nodal networks shown in Fig. 5(c).

We should emphasize that, due to the presence of glide mirror, there may exist a band switching between the two time reversal invariant momenta (TRIM), leading to the hourglass type dispersion. Taking the nodal ring on the $k_z = 0$ plane as an example, we have

$$G_z^4 = T_{310} = e^{-i3k_x}e^{-ik_y}. \tag{7}$$

Hence, the eigenvalues of G_z are dependent of k_x, k_y. At the Γ point, $g_z = \pm 1$. For this FM case, each spin channel can be regarded as a spinless case. Such that $\mathcal{T} = \mathcal{K}$, $\mathcal{K}$ is the conjugate complex operation, which leads to a Kramer degeneracy at the Γ point. Every Bloch state on plane $k_z = 0$ can be chosen as the eigenstate $|u\rangle$ of G_z; it shows a double degeneracy, $\{|u\rangle, \mathcal{T}|u\rangle\}$, at the Γ point. Notably, $|u\rangle$ have the same eigenvalue $g_z = +1$ (or $g_z = -1$) as its Kramer partner $\mathcal{T}|u\rangle$. However, one notes that at X $= (0, \pi, 0)$ (the coordinate in conventional cell) $g_z = \pm i$, each Kramer pair $|u\rangle$ and $\mathcal{T}|u\rangle$ shares the different eigenvalues g_z (one is $g_z = i$ and the other one is $g_z = -i$). Therefore, there must be a partner switching when going from Γ to X, leading to an hourglass band crossing. Furthermore, since $k_z = 0$ plane is invariant under glide mirror G_z, its eigenvalue g_z can be well defined on this plane. Such that the above discussion can be applied to any path on this plane and connecting the two TRIMs, we trace out an hourglass nodal loop on this plane. The same argument can be extended to HNL2 and HNL3 on planes k_{x-y} and k_{x-z}.

VII. DISCUSSIONS AND CONCLUSION

We have several remarks on the topological band structure of Mg_2VO_4. First, noticing the Mg_2VO_4 system preserves the inversion symmetry but lacks the time-reversal symmetry; the HNLs and hourglass networks are all time-reversal-breaking Weyl ones with the double degeneracy. These Weyl HNLs are different with the Dirac ones proposed in ReO_2 previously [86]. Second, the hourglass networks situate almost at the Fermi level and have a very clean band structure without interferential bands nearby; hence, their novel properties may be readily investigated in future experiments. Third, the hourglass networks arise from the bands in one single spin channel, thus the hourglass-network fermions are fully spin polarized. Such fully spin-polarized fermions can be meaningful for spintronics applications.

In addition, we want to point out that hourglass line-hourglass chain or hourglass net have already been proposed in spinless models [67] and in a few nonmagnetic materials such as oxide Ag_2BiO_3 [87,88]. However, similar research in the magnetic system is quite rare. Therefore, Mg_2VO_4 compound can be a good material platform to investigate the potential entanglement effects between hourglass fermions and magnetism. We also want to emphasize that the nodal chain states here are also fundamentally different than proposed in ferromagnetic Heusler compound Co_2MnGa [72], because the nodal chains in Co_2MnGa do not show the hourglass dispersion.

Another important feature for the Mg_2VO_4 system is that the hourglass networks have 100% spin polarization, because Mg_2VO_4 is a half metal and the conducting electrons purely originate from the bands in the same spin channel. Previously, it has also seen several reports on topological phases identified in half metals, such as the double Weyl phase in half metal $HgCr_2Se_4$ [89] and the Weyl half metal $Co_3Se_2S_2$ [90]. In addition, nodal line and nodal surface states with the 100% spin polarization have also been reported in several half metals such as $Li_3(FeO_3)_2$ compound [48], tetragonal β-V_2OPO_4[91], MnN monolayer [92], CrN monolayer [30], $CsCrX_3$ (X = Cl, Br, I) compounds [39], and some spinel materials [32,73]. Comparing with traditional topological materials, topological half metals with 100% spin polarization could be meaningful in spintronics applications.

In conclusion, we report the presence of fully spin-polarized hourglass networks in Mg_2VO_4 compound with the nonsymmorphic crystal symmetry. The hourglass networks are constructed by three HNLs, which form the conjunction among one inner nodal chain and two outer nodal chains. The hourglass networks are symmetry enforced and cannot be annihilated without breaking symmetries. Since the hourglass networks are solely formed by bands in the spin up channel, they have the 100% spin polarization. From this perspective, such nodal networks are different from those identified in nonmagnetic materials. The nodal networks show clear drumhead surface states, which are also fully spin polarized. The SOC impact on the nodal networks has been discussed. In addition, the fully spin-polarized nodal networks are found to be robust against the electron correlation effects and the lattice strain. Effective models are constructed, which can successfully describe the nature of hourglass networks. This work provides an excellent platform to investigate the hourglass fermions in the magnetic system, as well as bring potential applications in spintronics.

ACKNOWLEDGMENTS

This work is supported by National Natural Science Foundation of China (Grant No. 11904074), the National Natural Science Foundation of China (Grant No. 11835003), and Nature Science Foundation of Hebei Province (No. E2019202222 and No. E2019202107). One of the authors (X.Z.) acknowledges the financial support from Young Elite Scientists Sponsorship Program by Tianjin and the financial support from introduction overseas Scientists Sponsorship Program by Hebei Province.

[1] H. Weyl, Z. Phys. **56**, 330 (1929).
[2] C. Herring, Phys. Rev **52**, 365 (1937).
[3] S. Borisenko, Q. Gibson, D. Evtushinsky, V. Zabolotnyy, B. Buchner, and R. J. Cava, Phys. Rev. Lett. **113**, 027603 (2014).
[4] X. Wan, A. M. Turner, A. Vishwanath, and S. Y. Savrasov, Phys. Rev. B **83**, 205101 (2011).
[5] A. A. Burkov and L. Balents, Phys. Rev. Lett. **107**, 127205 (2011).
[6] M. Z. Hasan, S.-Y. Xu, I. Belopolski, and S.-M. Huang, Annu. Rev. Condens. Matter Phys. **8**, 289 (2017).
[7] H. Weng, C. Fang, Z. Fang, B. A. Bernevig, and X. Dai, Phys. Rev. X **5**, 011029 (2015).
[8] A. Bansil, H. Lin, and T. Das, Rev. Mod. Phys. **88**, 021004 (2016).
[9] Z. Wang, Y. Sun, X. Q. Chen, C. Franchini, G. Xu, H. Weng, X. Dai, and Z. Fang, Phys. Rev. B **85**, 195320 (2012).
[10] Z. K. Liu, B. Zhou, Y. Zhang, Z. J. Wang, H. M. Weng D. Prabhakaran, S.-K. Mo, Z. X. Shen, Z. Fang, X. Dai, Z. Hussain, and Y. L. Chen, Science **343**, 864 (2014).
[11] Y. Liu, Z.-M. Yu, C. Xiao, and S. A. Yang, Phys. Rev. Lett. **125**, 076801 (2020).
[12] B. Q. Lv, H. M. Weng, B. B. Fu, X. P. Wang, H. Miao, J. Ma, P. Richard, X. C. Huang, L. X. Zhao, G. F. Chen, Z. Fang, X. Dai, T. Qian, and H. Ding, Phys. Rev. X **5**, 031013 (2015).
[13] S.-Y. Xu, I. Belopolski, N. Alidoust, M. Neupane, G. Bian, C. Zhang, R. Sankar, G. Chang, Z. Yuan, C.-C. Lee *et al.*, Science **349**, 613 (2015).
[14] S. A. Yang, SPIN **06**, 1640003 (2016)
[15] A. C. Potter, I. Kimchi, and A. Vishwanath, Nat. Commun. **5**, 5161 (2014).
[16] K. Taguchi, T. Imaeda, M. Sato, and Y. Tanaka, Phys. Rev. B **93**, 201202(R) (2016).
[17] F. de Juan, A. G. Grushin, T. Morimoto, and J. E. Moore, Nat. Commun. **8**, 15995 (2017).
[18] Y. Chen, S. Wu, and A. A. Burkov, Phys. Rev. B **88**, 125105 (2013).
[19] P. Hosur and X.-L. Qi, Phys. Rev. B **91**, 081106(R) (2015).
[20] P. Goswami, G. Sharma, and S. Tewari, Phys. Rev. B **92**, 161110(R) (2015).
[21] J. Ma and D. A. Pesin, Phys. Rev. B **92**, 235205 (2015).
[22] A. A. Soluyanov, D. Gresch, Z. Wang, Q. Wu, M. Troyer, X. Dai, and B. A. Bernevig, Nature (London) **527**, 495 (2015).
[23] B. Bradlyn, J. Cano, Z. Wang, M. G. Vergniory, C. Felser, R. J. Cava, and B. A. Bernevig, Science **353**, aaf5037 (2016).
[24] S. Zaheer, S. M. Young, D. Cellucci, J. C. Y. Teo, C. L. Kane, E. J. Mele, and A. M. Rappe, Phys. Rev. B **87**, 045202 (2013).
[25] G. W. Winkler, Q. S. Wu, M. Troyer, P. Krogstrup, and A. A. Soluyanov, Phys. Rev. Lett. **117**, 076403 (2016).
[26] Z. Zhu, G. W. Winkler, Q. S. Wu, J. Li, and A. A. Soluyanov, Phys. Rev. X **6**, 031003 (2016).
[27] H. Weng, C. Fang, Z. Fang, and X. Dai, Phys. Rev. B **93**, 241202(R) (2016).
[28] L. Jin, X. Zhang, X. Dai, H. Liu, G. Chen, and G. Liu, J. Mater. Chem. C **7**, 1316 (2019).

[29] W. Meng, X. Zhang, T. He, L. Jin, X. Dai, Y. Liu, and G. Liu, J. Adv. Res. **24**, 523 (2020).

[30] T. He, X. Zhang, Y. Liu, X. Dai, G. Liu, Z.-M. Yu, and Y. Yao, Phys. Rev. B **102**, 075133 (2020).

[31] L. Jin, X. Zhang, Y. Liu, X. Dai, X. Shen, L. Wang, and G. Liu, Phys. Rev. B **102**, 125118 (2020)

[32] H. Zhang, X. Zhang, Y. Liu, X. Dai, G. Chen, and G. Liu, arXiv:2007.12842.

[33] S. A. Yang, H. Pan, and F. Zhang, Phys. Rev. Lett. **113**, 046401 (2014).

[34] H. Weng, Y. Liang, Q. Xu, R. Yu, Z. Fang, X. Dai, and Y. Kawazoe, Phys. Rev. B **92**, 045108 (2015).

[35] Y. Chen, Y. Xie, S. A. Yang, H. Pan, F. Zhang, M. L. Cohen, and S. Zhang, Nano Lett. **15**, 6974 (2015).

[36] C. Zhong, Y. Chen, Y. Xie, S. A. Yang, M. L. Cohen, and S. Zhang, Nanoscale **8**, 7232 (2016).

[37] Q.-F. Liang, J. Zhou, R. Yu, Z. Wang, and H. Weng, Phys. Rev. B **93**, 085427 (2016).

[38] X. M. Zhang, Z. M. Yu, Z. M. Zhu, W. K. Wu, S. S. Wang, X. L. Sheng, and S. A. Yang, Phys. Rev. B **97**, 235150 (2018).

[39] W. Wu, Y. Liu, S. Li, C. Zhong, Z.-M. Yu, X.-L. Sheng, Y. X. Zhao, and S. A. Yang, Phys. Rev. B **97**, 115125 (2018).

[40] Z.-M. Yu, W. Wu, X.-L. Sheng, Y. X. Zhao, and S. A. Yang, Phys. Rev. B **99**, 121106(R) (2019)

[41] Y. Kim, B. J. Wieder, C. L. Kane, and A. M. Rappe, Phys. Rev. Lett. **115**, 036806 (2015).

[42] R. Yu, H. Weng, Z. Fang, X. Dai, and X. Hu, Phys. Rev. Lett. **115**, 036807 (2015).

[43] X. M. Zhang, L. Jin, F. X. Dai, and G. D. Liu, J. Phys. Chem. Lett. **8**, 4814 (2017).

[44] T.-T. Zhang, Z.-M. Yu, W. Guo, D. Shi, G. Zhang, and Y. Yao, J. Phys. Chem. Lett. **8**, 5792 (2017).

[45] X. Sheng, Z.-M. Yu, R. Yu, H. Weng, and S. A. Yang, J. Phys. Chem. Lett. **8**, 3506 (2017).

[46] Z. Zhu, Y. Liu, Z.-M. Yu, S.-S. Wang, Y. X. Zhao, Y. Feng, X.-L. Sheng, and S. A. Yang, Phys. Rev. B **98**, 125104 (2018).

[47] X. M. Zhang, Z.-M. Yu, Y. H. Lu, X.-L. Sheng, H. Y. Yang, and S. A. Yang, Phys. Rev. B **97**, 125143 (2018).

[48] C. Chen, Z.-M. Yu, S. Li, Z. Chen, X.-L. Sheng, and S. A. Yang, Phys. Rev. B **99**, 075131 (2019).

[49] G. Bian, T.-R. Chang, R. Sankar, S.-Y. Xu, H. Zheng, T. Neupert, C.-K. Chiu, S.-M. Huang, G. Chang, I. Belopolski *et al.*, Nat. Commun. **7**, 10556 (2016)

[50] L. M. Schoop, M. N. Ali, C. Straber, A. Topp, A. Varykhalov, D. Marchenko, V. Duppel, S. S. P. Parkin, B. V. Lotsch, and C. R. Ast, Nat. Commun. **7**, 11696 (2016).

[51] M. Neupane, I. Belopolski, M. M. Hosen, D. S. Sanchez, R. Sankar, M. Szlawska, S.-Y. Xu, K. Dimitri, N. Dhakal, P. Maldonado, P. M. Oppeneer, D. Kaczorowski, F. Chou, M. Z. Hasan, and T. Durakiewicz, Phys. Rev. B **93**, 201104(R) (2016).

[52] D. Takane, Z. Wang, S. Souma, K. Nakayama, C. X. Trang, T. Sato, T. Takahashi, and Y. Ando, Phys. Rev. B **94**, 121108(R) (2016).

[53] C. Fang, H. M. Weng, X. Dai, and Z. Fang, Chin. Phys. B **25**, 117106 (2016).

[54] Y. Du, F. Tang, D. Wang, L. Sheng, E.-j. Kan, C.-G. Duan, S. Y. Savrasov, and X. Wan, npj Quantum Mater. **2**, 3 (2017).

[55] Q. Xu, R. Yu, Z. Fang, X. Dai, and H. Weng, Phys. Rev. B **95**, 045136 (2017).

[56] S. A. Parameswaran, A. M. Turner, D. P. Arovas, and A. Vishwanath, Nat. Phys. **9**, 299 (2013).

[57] J. A. Steinberg, S. M. Young, S. Zaheer, C. L. Kane, E. J. Mele, and A. M. Rappe, Phys. Rev. Lett. **112**, 036403 (2014).

[58] S. M. Young and C. L. Kane, Phys. Rev. Lett. **115**, 126803 (2015).

[59] H. Watanabe, H. C. Po, M. P. Zaletel, and A. Vishwanath, Phys. Rev. Lett. **117**, 096404 (2016).

[60] B. J. Wieder and C. L. Kane, Phys. Rev. B **94**, 155108 (2016).

[61] Y. Chen, H.-S. Kim, and H.-Y. Kee, Phys. Rev. B **93**, 155140 (2016).

[62] B.-J. Yang, T. A. Bojesen, T. Morimoto, and A. Furusaki, Phys. Rev. B **95**, 075135 (2017).

[63] A. Furusaki, Sci. Bull. **62**, 788 (2017).

[64] Z. Wang, A. Alexandradinata, R. J. Cava, and B. A. Bernevig, Nature (London) **532**, 189 (2016).

[65] J. Ma, C. Yi, B. Lv, Z. Wang, S. Nie, L. Wang, L. Kong, Y. Huang, P. Richard, P. Zhang *et al.*, Sci. Adv. **3**, e1602415 (2017).

[66] M. Ezawa, Phys. Rev. B **94**, 155148 (2016).

[67] L. Wang, S.-K. Jian, and H. Yao, Phys. Rev. B **96**, 075110 (2017).

[68] S. Kobayashi, Y. Yamakawa, A. Yamakage, T. Inohara, Y. Okamoto, and Y. Tanaka, Phys. Rev. B **95**, 245208 (2017).

[69] C. Zhong, Y. Chen, Z.-M. Yu, Y. Xie, H. Wang, S. A. Yang, and S. Zhang, Nat. Commun. **8**, 15641 (2017).

[70] W. Chen, H.-Z. Lu, and J.-M. Hou, Phys. Rev. B **96**, 041102(R) (2017).

[71] T. Bzdusek, Q. S. Wu, A. Ruegg, M. Sigrist, and A. A. Soluyanov, Nature (London) **538**, 75 (2016).

[72] G. Chang, S.-Y. Xu, X. Zhou, S.-M. Huang, B. Singh, B. Wang, I. Belopolski, J. Yin, S. Zhang, A. Bansil *et al.* Phys. Rev. Lett. **119**, 156401 (2017).

[73] W. Jiang, H. Huang, F. Liu, J.-P. Wang, and T. Low, Phys. Rev. B **101**, 121113(R) (2020).

[74] Y. Zhou, F. Xiong, X. Wan, and J. An, Phys. Rev. B **97**, 155140 (2018).

[75] G. Kresse and J. Hafner, Phys. Rev. B **49**, 14251 (1994).

[76] G. Kresse and J. Furthmüller, Phys. Rev. B **54**, 11169 (1996).

[77] J. P. Perdew, K. Burke, and M. Ernzerhof, Phys. Rev. Lett. **77**, 3865 (1996).

[78] H. J. Monkhorst and J. D. Pack, Phys. Rev. B **13**, 5188 (1976).

[79] V. I. Anisimov, J. Zaanen, and O. K. Andersen, Phys. Rev. B **44**, 943 (1991).

[80] S. L. Dudarev, G. A. Botton, S. Y. Savrasov, C. J. Humphreys, and A. P. Sutton, Phys. Rev. B **57**, 1505 (1998).

[81] Q. S. Wu, S. N. Zhang, H.-F. Song, M. Troyer, and A. A. Soluyanov, Comput. Phys. Commun. **224**, 405 (2018).

[82] W. Ruedorff and B. Reuter, Z Anorg Allg Chem. **253**, 194 (1947).

[83] F. Bosi, H. Skogby, R. A. Fregola, U. Hålenius, Am. Mineral. **101**, 580 (2016).

[84] M. Li, S. Zheng, B. Liu, S. Wang, D. B. Dreisinger, Y. Zhang, H. Du, and Y. Zhang, Miner. Process. Extr. Metall. Rev. **38**, 228 (2017).

[85] J. Heyd, G. E. Scuseria, M. Ernzerhof, Hybrid functionals based on a screened coulomb potential, J. Chem. Phys. **118**, 8207 (2003).

[86] S.-S. Wang, Y. Liu, Z.-M. Yu, X.-L. Sheng, and S. A. Yang, Nat. Commun. **8**, 1844 (2017).

[87] B. Fu, X. Fan, D. Ma, C.-C. Liu, and Y. Yao, Phys. Rev. B **98**, 075146 (2018).

[88] B. Singh, B. Ghosh, C. Su, H. Lin, A. Agarwal, and A. Bansil, Phys. Rev. Lett. **121**, 226401 (2018).

[89] G. Xu, H. Weng, Z. Wang, X. Dai, and Z. Fang, Phys. Rev. Lett. **107**, 186806 (2011).

[90] E. Liu, Y. Sun, N. Kumar, L. Muechler, A. Sun, L. Jiao, S.-Y. Yang, D. Liu, A. Liang, Q. Xu, J. Kroder, V. Sß, H. Borrmann, C. Shekhar, Z. Wang, C. Xi, W. Wang, W. Schnelle, S. Wirth, Y. Chen, S. T. B. Goennenwein, and C. Felser, Nat. Phys. **14**, 1125 (2018).

[91] Y. J. Jin, R. Wang, Z. J. Chen, J. Z. Zhao, Y. J. Zhao, and H. Xu, Phys. Rev. B **96**, 201102(R) (2017).

[92] S.-S. Wang, Z.-M. Yu, Y. Liu, Y. Jiao, S. Guan, X.-L. Sheng, and S. A. Yang, Phys. Rev. Materials **3**, 084201 (2019).